Nano Research 2017, 10(10): 3295–3302
DOI 10.1007/s12274-017-1542-2
Research Article

ISSN 1998-0124
CN 11-5974/O4

Highly uniform and nonlinear selection device based on trapezoidal band structure for high density nano-crossbar memory array

Qing Luo[1,2], Xiaoxin Xu[1,2], Hangbing Lv[1,2,3] (✉), Tiancheng Gong[1,2], Shibing Long[1,2], Qi Liu[1,2], Ling Li[1,2], and Ming Liu[1,2,3] (✉)

[1] *Key Laboratory of Microelectronics Devices & Integrated Technology, Institute of Microelectronics, Chinese Academy of Sciences, Beijing 100029, China*
[2] *University of Chinese Academy of Sciences, Beijing 100049, China*
[3] *Jiangsu National Synergetic Innovation Center for Advanced Materials (SICAM), Nanjing 211800, China*

Received: 29 November 2016
Revised: 15 February 2017
Accepted: 17 February 2017

© Tsinghua University Press and Springer-Verlag Berlin Heidelberg 2017

KEYWORDS
crossbar array,
selector,
trapezoidal barrier,
gradient oxygen concentration,
high uniformity

ABSTRACT

Crossbar array provides a cost-effective approach for achieving high-density integration of two-terminal functional devices. However, the “sneaking current problem”, which can lead to read failure, is a severe challenge in crossbar arrays. To inhibit the sneaking current from unselected cells, the integration of individual selection devices is necessary. In this work, we report a novel TaO_x-based selector exhibiting a trapezoidal band structure formed by tuning the concentration of defects in the oxide. Salient features such as a high current density (1 $MA\cdot cm^{-2}$), high selectivity (5×10^4), low off-state current (~10 pA), robust endurance ($>10^{10}$), self-compliance, and excellent uniformity were successfully achieved. The integrated one-selector one-resistor (1S1R) device exhibits high nonlinearity in the low resistance state (LRS), which is quite effective in solving the sneaking current issue.

1 Introduction

A passive crossbar array is a fundamental structure widely utilized for high-density storage [1–7], reconfigurable nonvolatile logic [8–12], and neuromorphic computing [13–16] applications. It is a sensible architecture suitable for two-terminal functional devices such as an atomic switch device [17, 18], phase change memory [19, 20], spin transfer torque device [21, 22], and CNT-based switching elements [23, 24] to achieve high-density integration with the smallest planar footprint and can possibly be stacked in three dimensions. However, the “sneaking current issue” caused by leakage from undesignated cells in a crossbar

Address correspondence to Hangbing Lv, lvhangbing@ime.ac.cn; Ming Liu, liuming@ime.ac.cn

array is a key problem, as illustrated in Fig. 1(a), which leads to read/write disturbance in memory operation and inaccuracy in logic computation.

To overcome this, integration of a two-terminal selection device exhibiting a high nonlinearity at each crosspoint node is necessary for configuring a one-selector one-resistor (1S1R) cell. The sneak current could thus be greatly alleviated due to the nonlinearity achieved with the selector device (Fig. 1(b)). Several functional materials such as perovskite ferroelectrics [25], doped oxide [26], mixed ionic electron conduction material [27], metal-insulator transition material [28, 29], and Schottky emission stacks [30, 31] have been investigated to configure a selector device. Some selection devices based on ion movement or local phase change [25–29] were examined, which provided an extremely high nonlinearity (>10^7), high on-current density (>10^7 A·cm^{-2}), and good scability. However, these devices exhibit a large variation in the threshold switching voltage, resulting in a limited voltage window for reading. As shown in Fig. S1 (in the Electronic Supplementary Material (ESM)), the read voltage window is highly dependent on the threshold switching voltage range ($\Delta V = V_{\text{th-max}} - V_{\text{th-min}}$). The minimum criterion of $\Delta V < V_{\text{th-min}}$ should be satisfied in order to guarantee a successful read operation in the case of the commonly used V/2 bias configuration. The line resistance makes the situation even worse (Fig. S2 in the ESM). On the contrary, Schottky emission stacks exhibit better uniformity, because of pure electron conduction and the absence of ion movement or structure modification occurring during the operation [30, 31]. However, the nonlinearity and on current density of the interface type selector are not as satisfying as that of a filamentary type device. Thus, the design of an ingenious selection device exhibiting both high uniformity and high nonlinearity is important.

In this study, a high performance selector device is proposed by employing the concept of trapezoidal barrier in order to achieve high uniformity and nonlinearity. Based on theoretical calculations, the trapezoidal band structure provides a higher nonlinearity as compared to the square band structure or crested band structure (with the barrier height peaking in the middle and decreasing in both ways). In order to create such a trapezoidal barrier, dynamical tuning of the concentration of defects in an oxide was employed as an effective method. Using TaO_x with a gradient oxygen concentration, a selection device with a trapezoidal band exhibiting a large on-current density (~1 MA·cm^{-2}), high nonlinearity (>5×10^4), and extremely low parameter deviation was obtained, which achieved better combination performance than other reported selection devices such as VO_2 [28], triple layer device

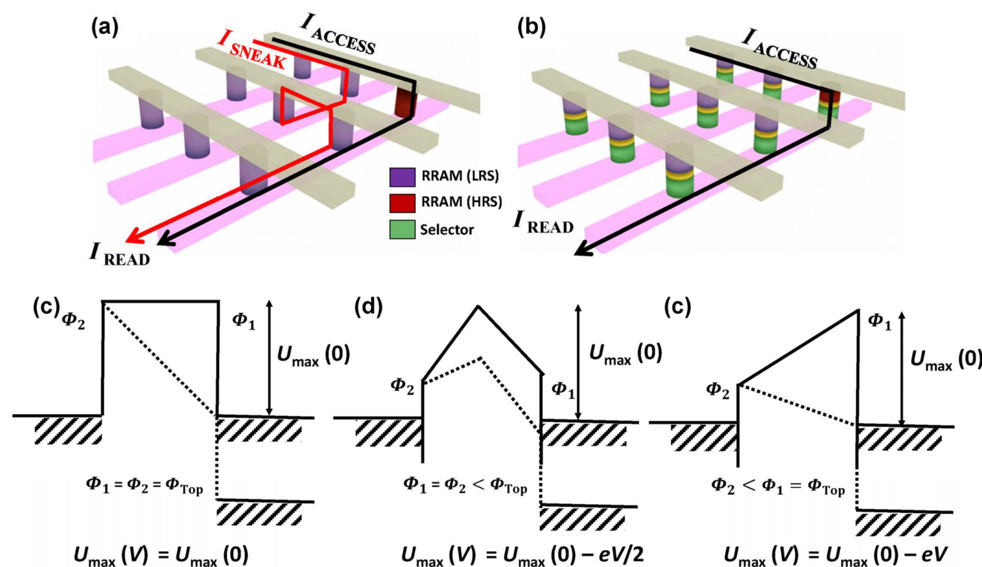

Figure 1 Conduction band diagrams of various tunnel barriers. (a) Sneak current in a crossbar array consisting of only memory cells and (b) without sneak current in a crossbar array with the 1S1R structure. (c) Typical uniform barrier, (d) idealized crested symmetric barrier, and (e) idealized trapezoidal energy barrier.

with a crested [31] band structure, and NbO_x [29]. The successful suppression of the leakage current was confirmed by measuring the fabricated 1S1R cell, suggesting that our novel selection device could open up a new pathway for realizing high-density three-dimensional (3D) resistive random access memory (RRAM) storage.

2 Experimental

W plug with a diameter of 1 μm subjected to chemical-mechanical planarization (CMP) was used as the bottom electrode (BE). Ta (8 nm) was deposited on the top of the W plug by magnetron sputtering at room temperature. A TaO_x layer was formed by rapid thermal annealing (RTA) carried out for 300 s in plasma O_2 by plasma enhanced chemical vapor deposition (PECVD) at 400 °C. Direct oxygen plasma with a power of 100 W was applied on the Ta film. After RTA, a Ru top electrode (TE) was deposited by sputtering at room temperature, followed by carrying out a lift-off process. The cell size was same as the superficial area of the W plug.

3 Results and discussion

The results of the theoretical calculations examining the maximum barrier height (U_{max}) in various tunnel barriers are shown in Figs. 1(c)–1(e). As compared with a uniform barrier, the highest part of the crested barrier (in the middle) is pulled down by the electric filed more quickly ($U_{max}(V) = U_{max}(0) - eV/2$), while $U_{max}(V)$ in the trapezoidal energy barrier changes faster ($U_{max}(V) = U_{max}(0) - eV$) than that in the crested barrier. Therefore, both the tunneling current and thermionic emission current can be significantly increased on applying an electric field in the trapezoidal energy barrier [32, 33]. This is helpful in designing a selection device with a high nonlinearity.

The implementation of a trapezoidal energy barrier was employed in composite semiconductors, where the barrier shaping could be achieved either by modulation doping [34] or by gradually changing the layer composition during epitaxy [33]. Another traditional method to form a trapezoidal energy barrier is to form ‘‘staircase’’ potential patterns, which requires complex fabrication processes [32]. Here, we propose a more favorable method to create the trapezoidal barrier by tuning the concentration of defects in oxides. In the oxidation process, plasma O_2 is directly applied on the surface of the Ta film continuously at 400 °C. This resulted in the production of a completely oxidative Ta surface. Under the surface, Ta cannot be in contact with O_2 directly. However, oxygen transfer from the surface to the interior of Ta film occurs, leading to a decrease of the oxygen. After annealing for a reasonable time (300 s), a gradient oxygen deficiency was achieved, as indicated in the cross-sectional transmission electron microscopy (TEM) image shown in Fig. 2(a) and the schematic in Fig. 2(b). Figure 2(c) shows the in-depth X-ray photoelectron spectroscopy (XPS) profile of TaO_x, indicating that the maximum intensity of oxygen peaks is present on the surface and the intensity gradually decreases towards the interior (Fig. 2(c)). The binding energy spectrum of the Ta 4f peaks is shown in Fig. 2(d). The feature peaks of $4f_{7/2}$ and $4f_{5/2}$ peaks of Ta^{5+} are located at 26.8 and 28.7 eV, respectively, and those of Ta^0 are located at 22.3 and 24.2 eV, respectively. On moving from the surface to the interior, the intensity of Ta^{5+} peaks decreases, whereas that of the Ta^0 peaks increases, indicating a gradient oxygen deficiency across TaO_x. The in-depth spectrum of the O 1s peaks shown in Fig. 2(e) further reinforces this observation. The band gap of TaO_x is highly dependent on the oxygen concentration, as revealed from the first-principles calculation results given in Fig. S3 in the ESM. Although the calculated band gap of TaO_x is lower than that obtained experimentally as previously reported in literature, it could be mainly caused due to the under estimation of the conduction band state energy in calculations. Thus, by creating a TaO_x system with a gradient oxygen concentration, the trapezoidal energy barrier with different barrier heights of $q\Phi_2$ and $q\Phi_1$ at the bottom and top interfaces could be successfully realized.

Figure 3(a) shows a typical *I*–*V* curve of the Ru/TaO_x/W selection device. Nonlinearity as high as 5×10^4 at 0.75 and 1.5 V, a high on-current density of > 1 $MA \cdot cm^{-2}$ (Fig. S4 in the ESM), and low leakage current in the pA range were achieved. The high performance and the asymmetric *I*–*V* curve of the selection device can be attributed to the thermionic

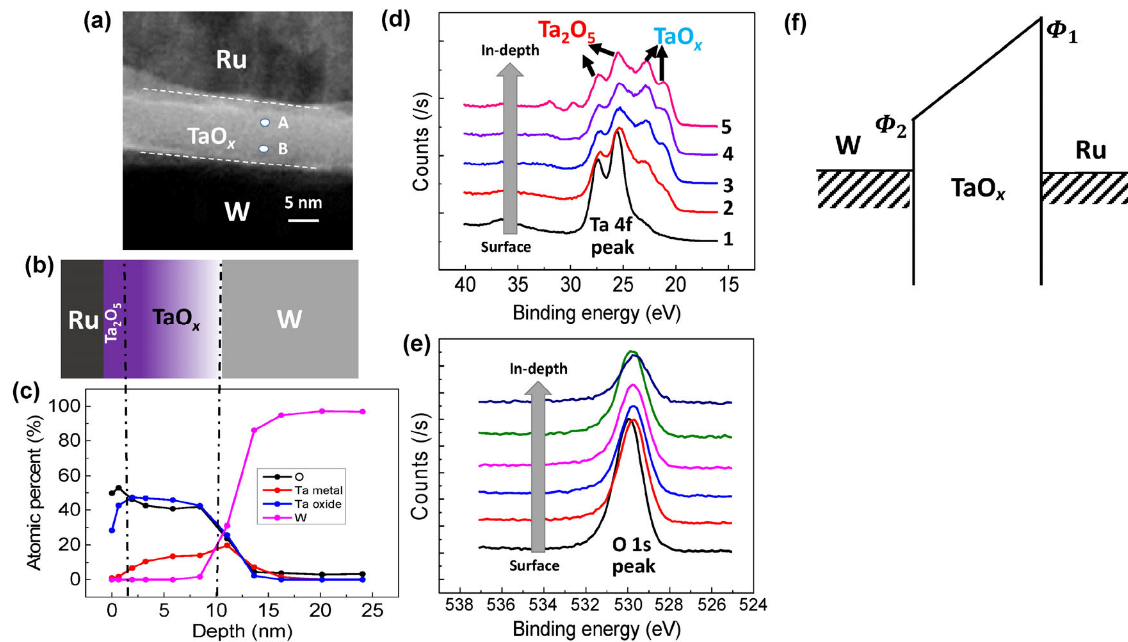

Figure 2 Trapezoidal band formation of the Ru/TaO_x/W structure. (a) The cross-sectional TEM image of the selector device. (b) Schematic illustration of concepts for the selector. (c) XPS depth-profile of the TaO_x/W stacks. (d) and (e) XPS spectra of the TaO_x film showing Ta and O peaks. (f) The band diagram of the Ru/TaO_x/W structure.

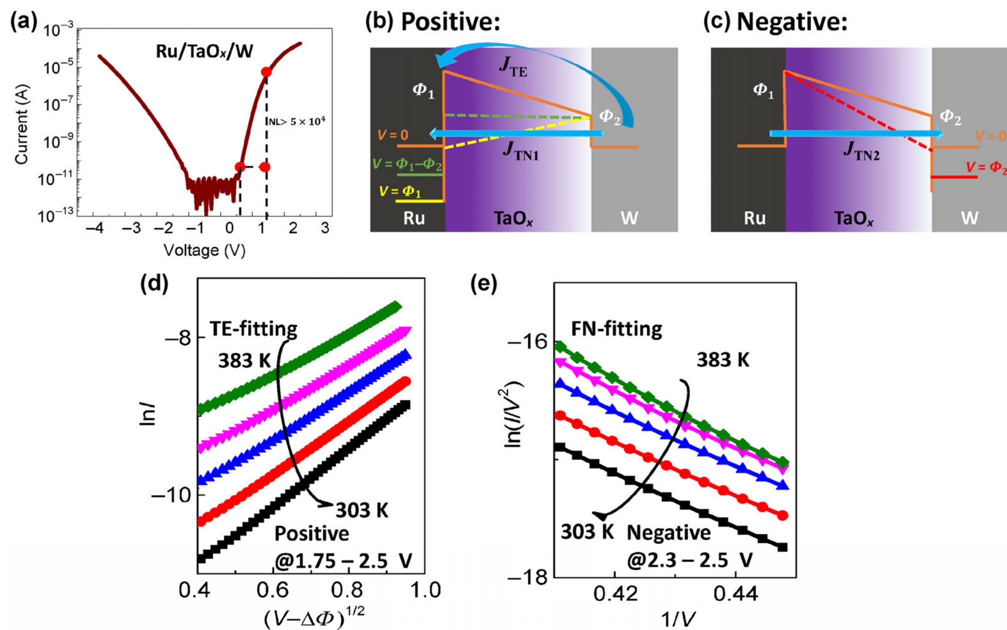

Figure 3 (a) Typical I–V curves of the selector device. (b) and (c) Schematic band diagram of the Ru/TaO_x/W structure under positive and negative bias conditions. (d) ln$I$ vs. $(V-\Delta\Phi)^{1/2}$ at different temperatures. (e) $\ln(I/V^2)$ vs. $1/V$ at different temperatures.

emission and tunneling emission achieved with the trapezoidal barrier model, as shown in Figs. 3(b) and 3(c). In this model, J_{TN} and J_{TE} are the net tunneling current density and thermionic emission current density, respectively. Considering that $q\Phi_2$ at the bottom interface is lower, thermionic emission is assumed to contribute to the electron transport associated with tunneling emission. In the case of a large positive bias, thermionic emission should be the dominant factor in electron conduction. To confirm this hypothesis, I–V

characteristics of the device were measured at different temperatures ranging from 303 to 383 K. The plot of ln$I$ vs. $(V–\Delta\Phi)^{1/2}$ in the voltage range of 1.75 to 2.5 V shown in Fig. 3(d) reveals a linear relationship at different temperatures that can be fitted well with the Simmons thermionic emission model [35, 36]. As the voltage applied on the positive side increases, the highest part of the energy band decreases sharply, leading to the increase of the tunneling current and thermionic emission current with a steep slope. Therefore, a high nonlinearity and high current density could be achieved at positive bias (Fig. 3(a)). Figure 3(c) shows the conduction mechanism of the device at negative bias. Because of the high energy barrier $q\Phi_1$, thermionic emission can be ignored and the electron transport is controlled by tunneling. In the negative region, as the voltage increases, the highest part of the energy barrier remains as $q\Phi_1$, resulting in a higher turn-on voltage than that observed in the positive side (Fig. 3(a)). Figure 3(e) shows the relation of $\ln(I/V^2)$ vs. $1/V$ at different temperatures, indicating the tunneling emission to be the dominant current mechanism at the negative bias region. This trapezoidal barrier model provides a guide for further device optimization.

To evaluate the uniformity of the selection device, a direct current (DC) cycling test was performed. Figure 4 shows the statistics indicating the uniformity achieved for different cycles and different devices. As shown in Fig. 4(a), each I–V curve almost overlaps after 10^3 successive DC cycles. The switching voltage is defined as the voltage at which the current reaches 10 nA. The probability of the turn-on voltage for 1,000 cycles is shown in Fig. 4(b). Excellent uniformity was achieved with an ultralow σ value of 0.01382 (σ is a parameter of the Gaussian distribution). Figures 4(c) and 4(d) show the statistics of the current at V_{READ} and $1/2V_{READ}$ values indicating a negligible standard deviation. To evaluate the device-to-device uniformity, 20 random devices were tested, and the corresponding I–V curves are plotted in Fig. S4 in the ESM. Figure 4(e) shows the cumulative probability of current at V_{READ} and $1/2V_{READ}$ in different devices, revealing excellent device-to-device uniformity. Furthermore, an ultralow standard deviation of the turn-on voltage values in different devices was achieved (Fig. 4(f)). Figure S5 in the ESM suggests that the Ru/TaO_x/W stack exhibits excellent reliability, making the selection device useful

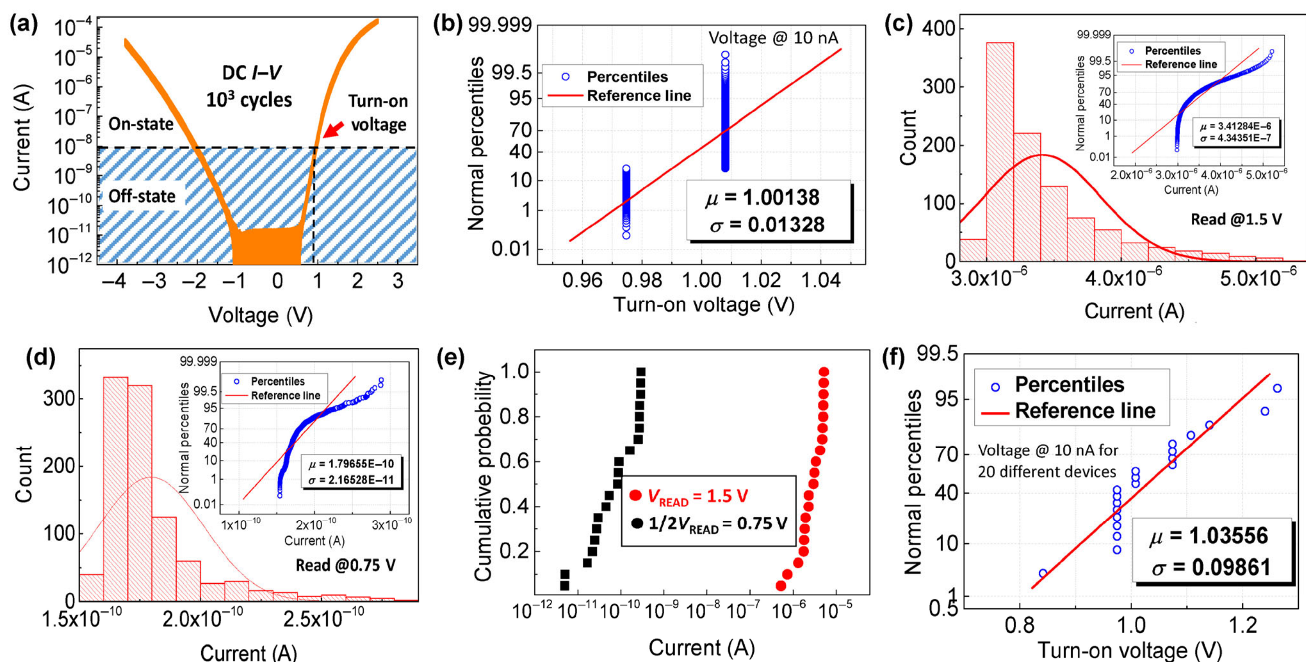

Figure 4 (a) 1,000 consecutive DC cycles of the selector device. (b) Cumulative probability of the turn-on voltage for 1,000 cycles. (c) Current statistics at 1.5 V. (d) Current statistics at 0.75 V. (e) Cumulative probability of current at V_{READ} and $1/2V_{READ}$ for different devices, demonstrating excellent device to device uniformity. (f) Cumulative probability of the turn-on voltage for 20 different devices.

for different applications. To confirm the large-scale feasibility, the selector device in 1 Kb cross-point array was fabricated and characterized (Fig. S6 in the ESM). A sufficient selectivity of ~10^3 with excellent uniformity was achieved.

To evaluate the effectiveness of the proposed selection device in suppressing the sneaking current in the crossbar array, we integrated the TaO_x selector with a Cu/HfO_2/Pt RRAM device by externally connecting to configure a 1S1R cell. Details of the fabrication process of the RRAM devices have been described elsewhere [37]. *I*–*V* curves of the 1S1R and 1R are shown in Fig. 5(a). The set voltage of the 1S1R device is <4 V and the reset voltage is <–5 V, which is much lower than that of a traditional flash memory. Hence, this operation voltage is acceptable for practical applications, which is comparable with the selector device with uniform barriers [30] and crested barriers [31]. The low resistance state (LRS) of the 1R device gives a linear *I*–*V* curve, whereas a nonlinearity of ~10^4 was achieved (1.8 V as V_{READ} and 0.9 V as $1/2V_{READ}$). Owing to the high uniformity of the selection device, the read region of the 1S1R structure corresponds to a wide range of 1.2–3.8 V (limited by the set voltage). As shown in Fig. 5(b), the nonlinear ratio depends on the read voltage. The read region for a nonlinearity of >10^3 is wide, from 1.2 to 2.4 V. Figure 5(c) shows the retention characteristics of the 1S1R device, indicating that negligible degradation of resistance is observed after 10^4 s thermal stress at 85 °C. To estimate the maximum array size of the 1S1R device, the read margin was calculated by considering a worst condition (*V* scheme with all the unselected devices at LRS) in an array (Fig. S7 in the ESM). Parameters for calculating the read margin were extracted from the *I*–*V* data of the 1S1R devices. As shown in Fig. 5(d), the read margin of the 1S1R structure was improved, as compared with the 1R structure. These results strongly suggest that the novel selection device could open up great opportunities to realize high-density 3D RRAM storage.

4 Conclusions

In summary, we demonstrated a highly uniform and nonlinear selection device by forming a trapezoidal

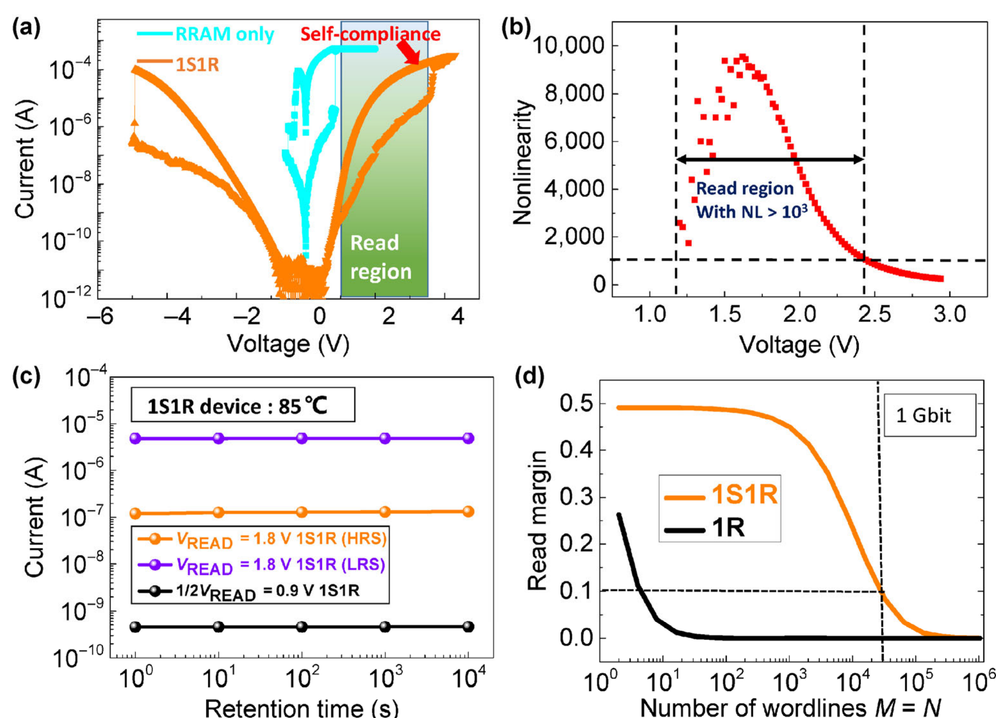

Figure 5 (a) Comparison of the *I*–*V* curves of the 1S1R and 1R. Up to a nonlinearity of 10^4 was achieved at LRS of the 1S1R structure. (b) Nonlinearity with different read voltages. (c) Retention characteristics of the 1S1R device at 85 °C. (d) Calculated read margin of the 1S1R devices under the worst condition.

energy barrier for high-density integration of two-terminal memory devices. To obtain a trapezoidal energy band, tuning of the concentration of defects in an oxide is proposed as a method, which offers a higher maximal barrier and simpler technological process as compared with the traditional method. Outstanding features such as a high nonlinearity, low off-state current, robust endurance, high uniformity, self-compliance, and excellent metal oxide semiconductor (CMOS) compatibility were achieved. Furthermore, the examination of the 1S1R device confirmed the feasibility of the formation of a selection device, suggesting that the Ru/TaO_x/W structure has a high potential in the large-scale manufacturing of crossbar arrays.

Acknowledgements

This work was supported by the National Key Research and Development Program of China (Nos. 2016YFA0203800 and 2016YFA0201803) and the National Natural Science Foundation of China (No. 61522408).

Electronic Supplementary Material: Supplementary material (details of the large variation caused problems, first-principles calculations for the band gap of TaO_x with different components, device to device uniformity, higher temperature performance of the selector and details for read margin calculation) is available in the online version of this article at https://doi.org/10.1007/s12274-017-1542-2.

References

[1] Waser, R.; Aono, M. Nanoionics-based resistive switching memories. *Nat. Mater.* **2007**, *6*, 833–840.

[2] Yu, S. M.; Chen, H. Y.; Gao, B.; Kang, J. F.; Wong, H. S. P. HfO_x-based vertical resistive switching random access memory suitable for bit-cost-effective three-dimensional cross-point architecture. *ACS Nano* **2013**, *7*, 2320–2325.

[3] Yang, J. J.; Pickett, M. D.; Li, X. M.; Ohlberg, D. A. A.; Stewart, D. R.; Williams, R. S. Memristive switching mechanism for metal/oxide/metal nanodevices. *Nat. Nanotechnol.* **2008**, *3*, 429–433.

[4] Xia, Q. F.; Yang, J. J.; Wu, W.; Li, X. M.; Williams, R. S. Self-aligned memristor cross-point arrays fabricated with one nanoimprint lithography step. *Nano Lett.* **2010**, *10*, 2909–2914.

[5] Tian, X. Z.; Wang, L. F.; Wei, J. K.; Yang, S. Z.; Wang, W. L.; Xu, Z.; Bai, X. D. Filament growth dynamics in solid electrolyte-based resistive memories revealed by *in situ* TEM. *Nano Res.* **2014**, *7*, 1065–1072.

[6] Sun, Y. H.; Yan, X. Q.; Zheng, X.; Liu, Y. C.; Shen, Y. W.; Zhang, Y. Influence of carrier concentration on the resistive switching characteristics of a ZnO-based memristor. *Nano Res.* **2016**, *9*, 1116–1124.

[7] Wu, Y.; Wei, Y.; Huang, Y.; Cao, F.; Yu, D. J.; Li, X. M.; Zeng, H. B. Capping $CsPbBr_3$ with ZnO to improve performance and stability of perovskite memristors. *Nano Res.* **2017**, *10*, 1584–1594.

[8] Wong, H. S. P.; Salahuddin, S. Memory leads the way to better computing. *Nat. Nanotechnol.* **2015**, *10*, 191–194.

[9] Xia, Q. F.; Robinett, W.; Cumbie, M. W.; Banerjee, N.; Cardinali, T. J.; Yang, J. J.; Wu, W.; Li, X. M.; Tong, W. M.; Strukov, D. B. et al. Memristor−CMOS hybrid integrated circuits for reconfigurable logic. *Nano Lett.* **2009**, *9*, 3640–3645.

[10] Cassinerio, M.; Ciocchini, N.; Ielmini, D. Logic computation in phase change materials by threshold and memory switching. *Adv. Mater.* **2013**, *25*, 5975–5980.

[11] Huang, P.; Kang, J.; Zhao, Y.; Chen, S.; Han, R.; Zhou, Z.; Chen, Z.; Ma, W.; Li, M.; Liu, L.; Liu, X. Reconfigurable nonvolatile logic operations in resistance switching crossbar array for large-scale circuits. *Adv. Mater.* **2016**, *28*, 9758–9764.

[12] Adam, G. C.; Hoskins, B. D.; Prezioso, M.; Strukov, D. B. Optimized stateful material implication logic for three-dimensional data manipulation. *Nano Res.* **2016**, *9*, 3914–3923.

[13] Lee, T. H.; Loke, D.; Huang, K. J.; Wang, W. J.; Elliott, S. R. Tailoring transient-amorphous states: Towards fast and power-efficient phase-change memory and neuromorphic computing. *Adv. Mater.* **2014**, *26*, 7493–7498.

[14] Yu, S. M.; Gao, B.; Fang, Z.; Yu, H. Y.; Kang, J. F.; Wong, H. S. P. A low energy oxide-based electronic synaptic device for neuromorphic visual systems with tolerance to device variation. *Adv. Mater.* **2013**, *25*, 1774–1779.

[15] Gao, B.; Bi, Y. J.; Chen, H. Y.; Liu, R.; Huang, P.; Chen, B.; Liu, L. F.; Liu, X. Y.; Yu, S. M.; Wong, H. S. P. et al. Ultra-low-energy three-dimensional oxide-based electronic synapses for implementation of robust high-accuracy neuromorphic computation systems. *ACS Nano* **2014**, *8*, 6998–7004.

[16] Wang, Z. R.; Joshi, S.; Savel'ev, S. E.; Jiang, H.; Midya, R.; Lin, P.; Hu, M.; Ge, N.; Strachan, J. P.; Li, Z. Y. et al. Memristors with diffusive dynamics as synaptic emulators for neuromorphic computing. *Nat. Mater.* **2017**, *16*, 101–108.

[17] Eigler, D. M.; Lutz, C. P.; Rudge, W. E. An atomic switch realized with the scanning tunnelling microscope. *Nature* **1991**, *352*, 600–603.

[18] Krishnan, K.; Tsuruoka, T.; Mannequin, C.; Aono, M. Mechanism for conducting filament growth in self-assembled polymer thin films for redox-based atomic switches. *Adv. Mater.* **2016**, *28*, 640–648.

[19] Simpson, R. E.; Fons, P.; Kolobov, A. V.; Fukaya, T.; Krbal, M.; Yagi, T.; Tominaga, J. Interfacial phase-change memory. *Nat. Nanotechnol.* **2011**, *6*, 501–505.

[20] Hegedüs, J.; Elliott, S. R. Microscopic origin of the fast crystallization ability of Ge-Sb-Te phase-change memory materials. *Nat. Mater.* **2008**, *7*, 399–405.

[21] Sankey, J. C.; Cui, Y.-T.; Sun, J. Z.; Slonczewski, J. C.; Buhrman, R. A.; Ralph, D. C. Measurement of the spin-transfer-torque vector in magnetic tunnel junctions. *Nat. Phys.* **2008**, *4*, 67–71.

[22] Liu, L. Q.; Pai, C.-F.; Li, Y.; Tseng, H. W.; Ralph, D. C.; Buhrman, R. A. Spin-torque switching with the giant spin hall effect of tantalum. *Science* **2012**, *336*, 555–558.

[23] Xiong, F.; Liao, A. D.; Estrada, D.; Pop, E. Low-power switching of phase-change materials with carbon nanotube electrodes. *Science* **2011**, *332*, 568–570.

[24] Bandaru, P. R.; Daraio, C.; Jin, S.; Rao, A. M. Novel electrical switching behaviour and logic in carbon nanotube Y-junctions. *Nat. Mater.* **2005**, *4*, 663–666.

[25] Jiang, A. Q.; Wang, C.; Jin, K. J.; Liu, X. B.; Scott, J. F.; Hwang, C. S.; Tang, T. A.; Lu, H. B.; Yang, G. Z. A resistive memory in semiconducting $BiFeO_3$ thin-film capacitors. *Adv. Mater.* **2011**, *23*, 1277–1281.

[26] Luo, Q.; Xu, X. X.; Liu, H. T.; Lv, H. B.; Gong, T. C.; Long, S. B.; Liu, Q.; Sun, H. T.; Banerjee, W.; Li, L. et al. Cu BEOL compatible selector with high selectivity ($>10^7$), extremely low off-current (~pA) and high endurance ($>10^{10}$). In *2015 IEEE International Electron Devices Meeting (IEDM)*, Washington, DC, 2015, pp 10.4.1–10.4.4.

[27] Gopalakrishnan, K.; Shenoy, R. S.; Rettner, C. T.; Virwani, K.; Bethune, D. S.; Shelby, R. M.; Burr, G. W.; Kellock, A.; King, R. S.; Nguyen, K. et al. Highly-scalable novel access device based on mixed ionic electronic conduction (MIEC) materials for high density phase change memory (PCM) arrays. In *2010 Symposium on VLSI Technology*, Honolulu, 2010, pp 205–206.

[28] Son, M.; Lee, J.; Park, J.; Shin, J.; Choi, G.; Jung, S.; Lee, W.; Kim, S.; Park, S.; Hwang, H. Excellent selector characteristics of nanoscale VO_2 for high-density bipolar ReRAM applications. *IEEE Electron Device Lett.* **2011**, *32*, 1579–1581.

[29] Kim, S.; Liu, X. J.; Park, J.; Jung, S.; Lee, W.; Woo, J.; Shin, J.; Choi, G.; Cho, C.; Park, S. et al. Ultrathin (<10 nm) Nb_2O_5/NbO_2 hybrid memory with both memory and selector characteristics for high density 3D vertically stackable RRAM applications. In *2012 Symposium on VLSI Technology (VLSIT)*, Honolulu, HI, 2012, pp 155–156.

[30] Huang, J.-J.; Tseng, Y.-M.; Hsu, C.-W.; Hou, T.-H. Bipolar $Ni/TiO_2/Ni$ selector for 1S1R crossbar array applications. *IEEE Electron Device Lett.* **2011**, *32*, 1427–1429.

[31] Lee, W.; Park, J.; Kim, S.; Woo, J.; Shin, J.; Choi, G.; Park, S.; Lee, D.; Cha, E.; Lee, B. H. et al. High current density and nonlinearity combination of selection device based on $TaO_x/TiO_2/TaO_x$ structure for one selector–one resistor arrays. *ACS Nano* **2012**, *6*, 8166–8172.

[32] Likharev, K. K. Layered tunnel barriers for nonvolatile memory devices. *Appl. Phys. Lett.* **1998**, *73*, 2137–2139.

[33] Allyn, C. L.; Gossard, A. C.; Wiegmann, W. New rectifying semiconductor structure by molecular beam epitaxy. *Appl. Phys. Lett.* **1980**, *36*, 373–376.

[34] Malik, R. J.; Aucoin, T. R.; Ross, R. L.; Board, K.; Wood, C. E. C.; Eastman, L. F. Planar-doped barriers in GaAs by molecular beam epitaxy. *Electron. Lett.* **1980**, *16*, 836–838.

[35] Simmons, J. G. Electric tunnel effect between dissimilar electrodes separated by a thin insulating film. *J. Appl. Phys.* **1963**, *34*, 2581–2590.

[36] Simmons, J. G. Potential barriers and emission-limited current flow between closely spaced parallel metal electrodes. *J. Appl. Phys.* **1964**, *35*, 2472–2481.

[37] Xu, X. X.; Lv, H. B.; Li, Y. X.; Liu, H. T.; Wang, M.; Liu, Q.; Long, S. B.; Liu, M. Degradation of gate voltage controlled multilevel storage in one transistor one resistor electrochemical metallization cell. *IEEE Electron Device Lett.* **2015**, *36*, 555–557.